Chinese Chemical Letters 33 (2022) 1298–1302

Contents lists available at ScienceDirect

Chinese Chemical Letters

journal homepage: www.elsevier.com/locate/cclet

# *In-situ* synthesis of N, S co-doped hollow carbon microspheres for efficient catalytic oxidation of organic contaminants

Yongbing Xie[a,b], Ya Liu[c,d], Yujie Yao[b,e], Yanchun Shi[b], Binran Zhao[e,*], Yuxian Wang[c,*]

[a] State Key Laboratory of Vanadium and Titanium Resources Comprehensive Utilization, Panzhihua 617000, China
[b] CAS Key Laboratory of Green Process & Engineering, Beijing Engineering Research Center of Process Pollution Control, Institute of Process Engineering, Chinese Academy of Sciences, Beijing 100190, China
[c] State Key Laboratory of Heavy Oil Processing, State Key Laboratory of Petroleum Pollution Control, China University of Petroleum-Beijing, Beijing 102249, China
[d] School of Chemical Engineering and Advanced Materials, The University of Adelaide, Adelaide, SA 5005, Australia
[e] School of Chemical Engineering, Northwest University, Xi'an 710069, China

ARTICLE INFO

*Article history:*
Received 14 May 2021
Revised 5 July 2021
Accepted 24 July 2021
Available online 31 July 2021

*Keywords:*
Metal-free catalysis
Hollow carbon microspheres
N, S co-doping
Catalytic ozonation
Singlet oxygen ($^1O_2$)

## ABSTRACT

Metal-free heteroatom doped nanocarbons are promising alternatives to the metal-based materials in catalytic ozonation for destruction of aqueous organic contaminants. In this study, N, S co-doped hollow carbon microspheres (NSCs) were synthesized from the polymerization products during persulfate wet air oxidation of benzothiazole. The contents of doped N and S as well as the structural stability were maneuvered by adjusting the subsequent $N_2$-annealing temperature. Compared with the prevailing single-walled carbon nanotubes, the $N_2$-annealed NSCs demonstrated a higher catalytic ozonation activity for benzimidazole degradation. According to the quantitative structure-activity relationship (QSAR) analysis, the synergistic effect between the graphitic N and the thiophene-S which redistributed the charge distribution of the carbon basal plane contributed to the activity enhancement of the $N_2$-annealed NSCs. Additionally, the hollow structure within the microspheres served as the microreactor to boost the mass transfer and reaction kinetics *via* the nanoconfinement effects. Quenching and electron paramagnetic resonance (EPR) tests revealed that benzimidazole degradation was dominated by the produced singlet oxygen ($^1O_2$) species, while hydroxyl radicals ($^•OH$) were also generated and participated. This study puts forward a novel strategy for synthesis of heteroatom-doped nanocarbons and sheds a light on the relationship between the active sites on the doped nanocarbons and the catalytic performance.

The intensively discharged phenolic and nitrogen-contained heterocyclic organic contaminants within the wastewater from chemical, coking and pharmaceutical industries jeopardize the health of both natural lives and human beings. Advanced oxidation processes (AOPs) relying on the powerful generated reactive species have been developed as the promising remediation technologies to completely destruct the aqueous organic contaminants [1–3]. Among AOPs, catalytic ozonation processes have attracted broad research interests and been widely exploited in the practical applications [4–6]. Metal-based heterogenous catalysts, especially the transition metal-based ones, such as $MnO_2$, $CoFe_2O_4$ and $MnO_2$/rGO have been proved as highly reactive for $O_3$ activation [7–9]. The redox cycles originated from multi-valence states and the rich surface acidic sites on the transition metal-based catalysts facilitate the adsorption of $O_3$ molecules and their subsequent activation to produce reactive oxygen species (ROS) for destruction of contaminants [10,11]. However, the secondary pollution induced by metal-leaching under the oxidative environment cannot be fully avoided when metal oxides were used.

Metal-free carbocatalysts as the capable alternatives to the transitional metal oxides circumvent the metal leaching. Additionally, the adjustable structures of the carbocatalysts offer a versatile platform for tuning the reactivities [12,13]. Compared with bulky carbons such as activated carbon and biochar-based carbon materials with micropore-dominant structure, nanocarbons with inherent mesopores and macropores expediate the diffusion of both $O_3$ and the organics and thus accelerate their interactions with the active sites [14,15]. Recent years, metal-free nanocarbons with different dimensions have been synthesized and employed as the effective ozonation catalysts for destructing the aqueous organic contami-

---

* Corresponding authors.
*E-mail addresses:* zhaobr@nwu.edu.cn (B. Zhao), yuxian.wang@cup.edu.cn (Y. Wang).

https://doi.org/10.1016/j.cclet.2021.07.055

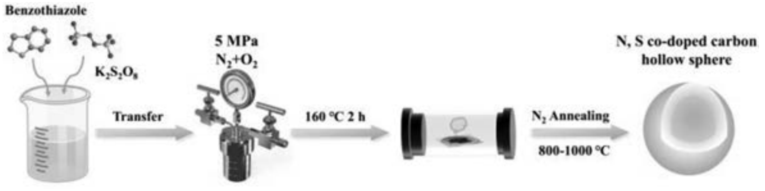

**Scheme 1.** Synthesis route for NSCs.

nants [5]. It is revealed that the catalytic activities of the nanocarbons are closely related with their surface chemistry. Defective sites and the surface oxygen functionalities are the key active sites for interacting with $O_3$ to produce ROS [16,17]. However, like the metal-based catalysts, the surface chemistry even the carbon skeleton of the nanocarbons can be altered by the powerful oxidative species during the catalytic ozonation reactions, resulting in the irreversible passivation.

Doping metal-free heteroatoms within the nanocarbon structure can increase the reactivity and the stability [18,19]. Both the charge and spin density of the carbon basal plane would be redistributed owing to the differences in electronegativity and the radius between the incorporated heteroatoms and the C atoms [20]. As the result, different oxidation regimes would be initiated depending on electron density distribution [21]. The synergistic effect arising from the co-doping different heteroatoms further regulates the charge distribution. Co-doping S atoms together with N atoms enlarges the electron-sparse regions of the C atoms adjacent to the doped N species, favoring the nucleophilic attack of the $O_3$ [22]. Furthermore, the unbalanced electron distribution also serves as the electron-mediator to protect the surface of the catalyst from over-oxidizing by the oxidative species during the catalytic reactions.

Herein, N and S co-doped hollow-structured carbon microspheres (NSCs) were prepared from the polymers generated during persulfate wet air oxidation (PWAO) of benzothiazole [23]. During this process, both N and S atoms were *in-situ* doped within the polymeric microspheres and their compositions were further regulated by the $N_2$ annealing at different temperatures (Scheme 1). Catalytic ozonation activities of the $N_2$-annealed NSCs were evaluated by utilizing benzimidazole (BMZ) as the target pollutants. The influencing factors such as solution pH and inorganic anions on catalytic performance were also investigated. The potential active sites and their correlations with the catalytic activities were analyzed by a quantitative structure-activity relationship (QSAR) analysis. In addition, a combined study of quenching and electron paramagnetic resonance (EPR) tests were performed to unveil the generated ROS and their possible roles in NSCs/$O_3$ system for benzimidazole degradation.

During PWAO of benzothiazole under high temperature (160 °C) and high pressure (5 MPa), hollow polymeric microspheres (NSC-Poly) were formed along with degradation, with the average diameter around 1 µm and the shell thickness of 200 nm (Fig. 1A). Annealing the NSC-Poly in $N_2$ at elevated temperature (800–1000 °C) maintained the hollow structure and the size of the microspheres (Figs. 1B and C). High-resolution transmittance electron microscope (HRTEM) observation in Fig. 1D further revealed that a greater graphitization degree was achieved by annealing in $N_2$ at 1000 °C (NSC-1000) by detecting some *quasi*-graphene lattices formed at the edge of the carbon shell.

The improvement of the graphitic degree after high-temperature $N_2$ annealing also reflected in the X-ray diffraction (XRD) patterns (Fig. 2A). Compared with NSC-Poly, NSC-800 annealing at 800 °C possessed a discernable characteristic (101) diffraction peak for graphitic carbon. The appearance of the characteristic C-N and C=S transmittance peaks in the Fourier transform infrared spectroscopy (FTIR) suggested that both N and S atoms were *in-situ* doped within the graphitic carbon lattice (Fig. 2B) [22]. X-ray photoelectron spectroscopy (XPS) analysis (Table S1 and Fig. S1 in Supporting information) and elemental analysis (Fig. 2C) were then performed to reveal the variations in the elemental composition of the NSCs after $N_2$-annealing. Compared with NSC-Poly, both XPS full surveys and the elemental analysis suggested that $N_2$ annealing significantly decreased the compositions of S (from 18 wt% to 5–8 wt%), O (from 16 wt% to $\sim$ 4 wt%), and H (from 5 wt% to trivial) within the structure and enhanced the C composition. Additionally, elevating the annealing temperature further decreased both the N and S doping amounts. Interestingly, for the $N_2$ annealed NSCs, the slightly decreased amount of the dopants did not reflect in the reduction of the defective level as $N_2$ annealing temperature increased. As illustrated in Raman spectra in Fig. 2D, NSCs annealing at different

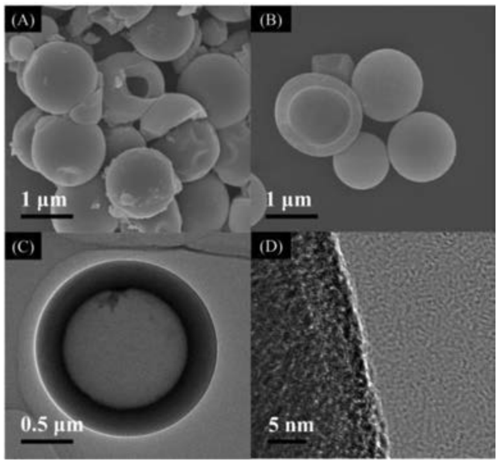

**Fig. 1.** SEM images of NSC-Poly (A) and NSC-1000 (B); TEM (C) and the corresponding HRTEM observations (D) of NSC-1000.

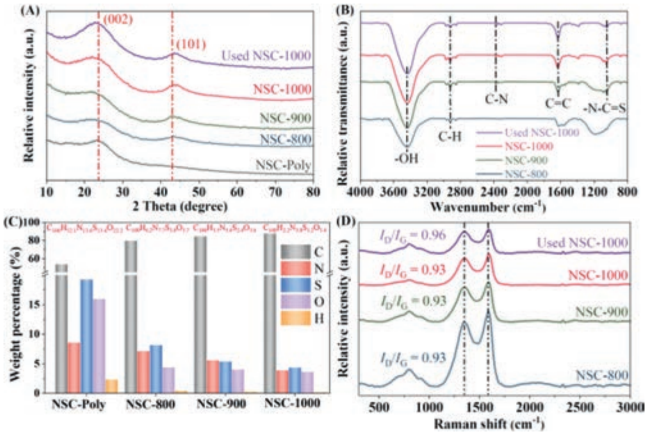

**Fig. 2.** XRD patterns (A), FTIR (B), element compositions (C) and Raman (D) spectra of the as-synthesized NSCs.

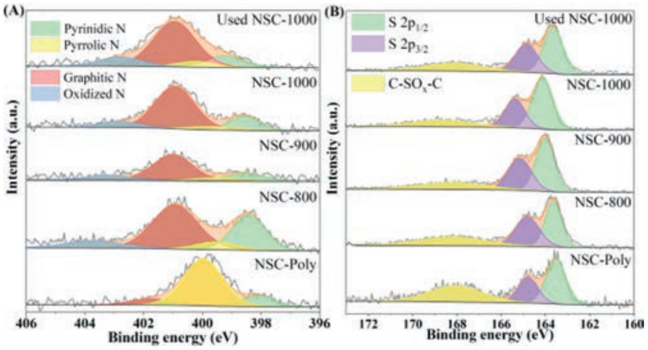

**Fig. 3.** High resolution XPS spectra on N 1s (A) and S 2p (B) surveys and the corresponding deconvolution results.

temperatures obtained similar intensity ratios of defective band to graphitic band ($I_D/I_G$).

High resolution XPS surveys on C 1s, N 1s and S 2p of the NSCs were performed and deconvoluted to investigate the detailed alterations in the surface chemistry under different treatments. For high resolution XPS surveys on C 1s, less than 10% variations were observed for sp$^2$/sp$^3$ ratios of $N_2$ annealed NSCs (Table S2 and Fig. S2 in Supporting information). Considering the large inherent error in deconvolution process, it is suggested that insignificant variations in defective levels of NSCs upon annealing at different temperatures were observed, which were in line with the Raman results. Furthermore, trivial changes in surface oxygen functionalities were discerned for the annealed NSCs. Different from C 1s species, substantial variations occurred to the doped N species for NSCs samples (Fig. 3A and Table S3 in Supporting information). After $N_2$ annealing, the dominant doped N species in NSCs shifted from the pyrrolic N to graphitic N. Additionally, further increasing the annealing temperature resulted in the enhancement of the graphitic N content. It is suggested that the high temperature annealing in the inert atmosphere favored the transformation of pyrrolic N into the graphitic N [24]. For doped S species, two main peaks were observed in the high resolution XPS S 2p surveys (Fig. 3B and Table S4 in Supporting information). The peak situated at 168.2 eV could be assigned to C-SO$_x$-C ($x$ = 2, 3, 4) groups [25], and the other peak can be deconvoluted into two characteristic peaks, corresponding to the S 2p$_{1/2}$ and S 2p$_{3/2}$ of the thiophene-S, respectively [26]. Compared with NSC-Poly, the $N_2$ annealed NSCs obtained much reduced C-SO$_x$-C contents, validating the significant decrease in the S-doping amounts after $N_2$ treatment. Meanwhile, increasing the $N_2$ annealing temperature enhanced the composition of S 2p$_{1/2}$.

Adsorption tests were performed prior to investigate the catalytic activities of the NSCs. NSCs displayed marginal adsorption capacities towards the BMZ at the ambient pH of 6.7 (Fig. S3 in Supporting information), though they obtained high specific surface areas (Table S5 and Fig. S4 in Supporting information). The charge difference between catalyst surface and the organics can significantly affect the adsorption capacity [5]. In accordance with the zeta potential measurements, the pH point of zero charges (pH$_{\text{pzc}}$) for NSC-Poly, NSC-800, NSC-900 and NSC-1000 were determined as 5.4, 4.6, 4.1, and 3.8, respectively. Decreasing the amount of surface oxygen functionalities by elevating the annealing temperature resulted in the abatement in pH$_{\text{pzc}}$, which agrees with our previous study [27]. With the ambient pH of 6.7, the surface of the NSCs was negatively charged. Therefore, the resulted electrostatic repulsion between the surface of the catalyst and the deprotonated BMZ molecules (p$K_a$ of 5.5) hindered the adsorption process. BMZ removal by ozonation alone was also set as the benchmark (Fig. S5 in Supporting information). Ozonation alone resulted in the 80% BMZ within 60 min, giving rise to the *pseudo*-first order reaction rate of 0.027 min$^{-1}$ (Fig. 4A). Utilizing NSC-Poly as the catalyst slightly increased the BMZ degradation efficiency with reaction rate of 0.032 min$^{-1}$. $N_2$ annealing further improved the catalytic ozonation activities of NSCs. Moreover, the catalytic performance enhanced as the $N_2$ annealing temperature increased. For NSC-1000, complete BMZ degradation was achieved within 45 min, resulting in a rate constant of 0.06 min$^{-1}$. Compared with other nanocarbons, the special hollow structure within the microspheres facilitated the exposure of higher amount of the reactive sites by enhancing the specific surface area. Furthermore, it created a confined space which acted as the nano/micro reactors that accelerated the mass and charge transfer and boosted the reaction kinetics [28]. Catalytic ozonation activity of commercial-obtained single-walled carbon tubes (SWCNTs) for BMZ degradation was also evaluated and a *pseudo*-first order reaction rate constant of 0.049 min$^{-1}$ was resulted. Therefore, the as-synthesized NSC-1000 as the byproducts of the PWAO treatments outperformed the cost-intensive SWCNTs in BMZ degradation.

Mineralization rates of BMZ were further monitored by time-dependent total organic carbon (TOC) abatements (Fig. S6 in Supporting information). NSC-Poly demonstrated a poor structural stability under the oxidative environment created by $O_3$ and the generated ROS, and an increased TOC was observed with the prolonged treatment time. $N_2$ annealing helped the construction of an outer graphitic shell which protected the attack of the oxidative species and thus increased the structural integrity of the catalysts. For NSC-1000, around 60% of the initial TOC was mineralized after 90 min. The robust structure of the $N_2$ annealed NSCs was also reflected by a high recyclability (Fig. 4B). A minor passivation was observed in the 3rd usage when NSC-1000 as employed and the catalytic activity could be recovered by a facile low-temperature annealing process.

Defective sites within the nanocarbons have been regarded as the potential active sites in catalytic reactions because they disturb the homogeneity of the carbon skeleton and tune the electronic status by the dangling bonds with unpaired electrons [5]. In this study, although $N_2$ annealing created higher number of defective sites on NSCs compared with NSC-Poly, the $N_2$-annealed samples at different temperatures obtained similar $I_D/I_G$ ratios, suggesting the defective level might not be the predominant factor influencing the catalytic activities of the $N_2$-annealed NSCs. Incorporating N atoms within the carbon skeleton can drastically alter the charge and spin density distribution around the doped area because of the large electronegativity difference between N and C (3.04 *vs.* 2.55) [29]. The edge-located pyridinic N and the graphitic N doping zone were the potential active sites facilitating the $O_3$ adsorption and its subsequent dissociation into ROS [21,27]. And the catalytic activities of the N-doped nanocarbons often demonstrated positive correlations with the relative contents of the pyridinic N and/or graphitic N. In this study, the surface N contents decreased with the increase of the annealing temperature. Additionally, deconvolution results of the high resolution XPS surveys on N 1s suggested that a higher amount of graphitic N was formed at the elevated temperature. By correlating the relative graphitic N contents with the pseudo-first order reaction rate constants, a good linearity was observed for the fitted line, suggested the key role of graphitic N (Fig. 4C). For S-doping, the relatively small difference in electronegativity between S and C (2.58 *vs.* 2.55) resulted in an insignificant charge redistribution; however, the S atom with a large radius could induce the deformation of the carbon skeleton when incorporated, resulting in the positively charged in the adjacent C atoms, especially for the thiophene-S [26]. The positively charged adjacent C atoms favored the nucleophilic attack of the peroxide-based oxidants and resulted in the nonradical pathway. The detailed ROS generation will be discussed in the following section.

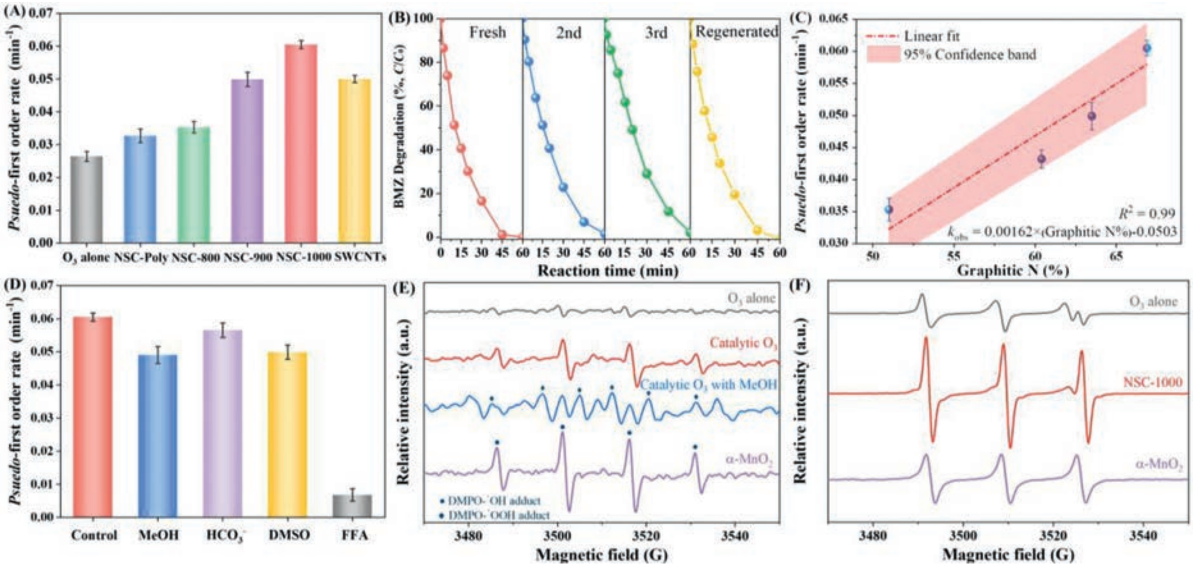

**Fig. 4.** (A) *Pseudo*-first order reaction rate constants plot for BMZ degradation by different treatments. (B) Reusability and regeneration tests for NSC-1000. (C) Linear regression fit between graphitic N contents and the *pseudo*-first order reaction rate constants for catalytic ozonation of BMZ with NSCs as catalysts. (D) Comparison of *pseudo*-first order reaction rate constants of quenching tests in catalytic ozonation by NSC-1000 utilizing BMZ as the target pollutants. EPR spectra with DMPO (E) and TEMP (F) as the spin trapping agents. Ozone flow rate: 100 mL/min; Ozone concentration: 25 mg/L; Catalyst loading: 0.1 g/L; Temperature: 25 °C; [BMZ]$_0$: 50 mg/L; Concentration of the scavengers: [MeOH]: 10 mmol/L, [$HCO_3^-$]=[DMSO]=[FFA]: 1 mmol/L; Initial solution pH was adjusted to 6.7 by diluted $H_2SO_4$ and NaOH.

Therefore, N and S doping sites could initiate the synergistic effect that greatly accelerated the electron transfer process between the surface of the catalyst and the adsorbed $O_3$ molecules and promoted the catalytic activity.

To investigate the possibly generated ROS and their contributions to BMZ degradation, a combined scavenging and *in-situ* electron paramagnetic resonance (EPR) tests were performed. Methanol (MeOH) and bicarbonate anion ($HCO_3^-$) were selected as the $^{\bullet}$OH scavengers to quench the $^{\bullet}$OH in both bulk solution and on the surface of the catalyst ($k_{^{\bullet}OH} = 9.7 \times 10^8$ L mol$^{-1}$ s$^{-1}$ and $8.5 \times 10^6$ L mol$^{-1}$ s$^{-1}$, respectively) [30-33]. As displayed in Fig. 4D, marginal quenching effects were observed with the presence of these scavengers. Further increasing the MeOH dosage only resulted in a slight increase in inhibitory effect (Fig. S7 in Supporting information). These observations revealed the minor contribution of free and surface-confined $^{\bullet}$OH to BMZ degradation. After from $^{\bullet}$OH-based oxidation, some recent studies also reported the nonradical oxidations of the organics based on the surface-adsorbed activated species such as surface-absorbed O ($^*O_{ad}$) and surface-activated $O_3$ complex [4]. Dimethyl sulfoxide (DMSO) possessing the high affinity towards the surface-adsorbed activated species but recalcitrant to $O_3$ attack (0.42 L mol$^{-1}$ s$^{-1}$) was added to evaluate their possible contributions to BMZ degradation [34]. A similar reaction rate to that of addition of MeOH was achieved when DMSO was involved within the catalytic oxidation, suggesting that the insignificant role of surface-adsorbed activated species in degrading BMZ. Singlet oxygen ($^1O_2$) with the moderate reduction potential (~ 0.85 V) obtained the selective oxidation behavior towards phenolic and unsaturated heterocyclic organics [35,36]. Addition of furfuryl alcohol (FFA) which obtains a fast reaction kinetic with $^1O_2$ ($1 \times 10^8$ L mol$^{-1}$ s$^{-1}$) resulted in a significant decrease in the reaction rate [37]. Noted that FFA is also an effective $^{\bullet}$OH scavenger. Considering the minor inhibitory effect brought by both the organic and inorganic $^{\bullet}$OH scavengers, the strong suppression effect with the addition of FFA mainly originated from the effect of $^1O_2$.

*In-situ* EPR experiments utilizing 5,5-dimethyl-1-pyrroline (DMPO) and 4-hydroxyl-2,2,6,6-tetramethyl-4-piperidine (TEMP) as spin trapping agents were then conducted to unravel the types of the generated ROS. Trace DMPO-$^{\bullet}$OH adducts with the hyperfine splitting couplings $a_N = a_H = 14.9$ G were discerned for ozonation alone (Figs. 4E and Fig. S8 in Supporting information). The involvement of NSC-1000 as the catalyst enhanced the signal intensities of the DMPO-$^{\bullet}$OH adducts, yet they were still significantly lower than those produced by $\alpha$-$MnO_2$ which is a well-recognized catalyst initiating $^{\bullet}$OH-based oxidations in catalytic ozonation [38]. Furthermore, the much inferior catalytic ozonation activity of $\alpha$-$MnO_2$ to that of NSC-1000 indicated that $^{\bullet}$OH was not the dominant ROS in NSC-1000/$O_3$ system for BMZ degradation (Fig. S9 in Supporting information). Superoxide radical ($HO_2^{\bullet}/O_2^{\bullet -}$) was also detected with the appearance of characteristic signal of DMPO-$^{\bullet}$OOH adducts. However, the recalcitrant BMZ is unlikely to be degraded by $HO_2^{\bullet}/O_2^{\bullet -}$ because of its weak oxidation capacity [39]. $HO_2^{\bullet}/O_2^{\bullet -}$ is more possibly to act as the key radical chain reaction intermediate for generating and evolving into other ROS. 4-hydroxyl-2,2,6,6-tetramethyl-4-piperidine (TEMP) prepared in MeOH solution was used as the spin trapping agent for $^1O_2$ detection by eliminating the influence of $^{\bullet}$OH [40]. Compared with ozonation, catalytic ozonation with the presence of NSC-1000 drastically boosted the signal intensity of the triplet TEMPO signals ($a_N = 16.9$ G), suggesting a greater amount of $^1O_2$ was produced (Fig. 4F). Additionally, the as-resulted TEMPO signal intensity for NSC-1000/$O_3$ system was higher than that in $\alpha$-$MnO_2$/$O_3$ system. Combining with the results of the quenching tests, it was thus proposed that $^1O_2$ was the dominant ROS for BMZ degradation.

Previous efforts suggested that graphitic N would induce a nonradical oxidation process based on the electron transfer between the adsorbed $O_3$ and the organic pollutants [21,41]. In this study, the co-doped S might further influence the charge and spin distribution of the carbon basal plane, creating a more electron-deficient zone on the adjacent C atoms due to the electronegativity and radius differences between the doped heteroatoms and the C atoms. Therefore, $O_3$ favored the nucleophilic attack on the electron-deficient zone and resulted in the formation of $^1O_2$ [42]. On the other hand, other active sites with unpaired and lone-pair electrons such as the defective sites and the pyridinic N sites can also initiate the radical-based oxidation pathways, though at low yield.

Apart from $HCO_3^-$, effects of the other inorganic anions which extensively exist in the real wastewater on catalytic performance were investigated (Fig. S10). The presence of $Cl^-$ (10 mmol/L) as the $^\bullet OH$ scavenger ($k_{^\bullet OH} = 4.3 \times 10^9$ L mol$^{-1}$ s$^{-1}$) suppressed the BMZ degradation efficiency and the resulted rate constant was less than those with the addition of MeOH and $HCO_3^-$. It is suggested that $Cl^-$ can also react with $^1O_2$ and $O_3$ to form the secondary chlorine species such as $Cl^\bullet$ and $Cl_2^{\bullet-}$ with inferior oxidation abilities and thus reduced the degradation efficiency [43]. $SO_4^{2-}$ has also been reported as the $^\bullet OH$ quenching agent and the addition of which gave rise to similar decreased rate constant to that of $HCO_3^-$ [43]. The presence of $PO_4^{3-}$ and $NO^{3-}$ slightly hindered the degradation efficiency. Apart from acting as the radical scavengers, these inorganic anions increased the ionic strength of the reaction solution and declined both solubility and mass transfer rate of $O_3$.

Effect of solution pH on BMZ degradation efficiency was also investigated utilizing the most reactive NSC-1000 as the catalyst (Fig. S11 in Supporting information). A general trend can be observed that increasing the solution pH resulted in the increase of both ozonation and catalytic ozonation treatment efficiency. The rate constant ratio of catalytic ozonation to ozonation alone enhanced from 1.27 to 2.83 as the solution pH elevated. Meanwhile, greater TOC mineralization rates were achieved at alkaline solution pH (Fig. S11 in Supporting information). A "substrate-dependent" oxidation behavior of the generated ROS during the catalytic ozonation for degradation of the organics has been revealed by the previous studies [27,41]. The produced $^1O_2$ with moderate oxidation ability would selectively attack the phenolic and the heterocyclic organics with unsaturated structures, while the generated $^\bullet OH$ favored the destruction of aliphatic acids and was responsible for the abatement of TOC. Therefore, the increased TOC mineralization rates at elevated pH ranges can be ascribed to the enhanced production of $^\bullet OH$ originated from alkaline activation of $O_3$. Furthermore, the boosted generation of $^\bullet OH$ might also induce the synergistic effect for the enhanced production of other ROS and thus improved the degradation efficiency.

In summary, N and S co-doped hollow carbon microspheres were successfully synthesized via catalytic polymerization process of benzothiazole during the PWAO and the compositions of doped N and S were tuned by the $N_2$ annealing. Compared with the NSC-Poly, the $N_2$-annealed NSCs obtained improved catalytic ozonation activities for BMZ degradation and greater structural stabilities. The synergistic effect between the graphitic N and the thiophene-S redistributed the charge density of the carbon basal plane and induced the $^1O_2$-dominant oxidation pathway.

## Declaration of competing interest

The authors declare no competing financial interest.

## Acknowledgments

The authors greatly appreciate the financial supports from the National Natural Science Foundation of China (No. 21978324), Tianjin Municipal Science and Technology Bureau (No. 18YFYSZ00170), Beijing Natural Science Foundation (No. 8192039), and Science Foundation of China University of Petroleum, Beijing (No. 2462020YXZZ034).

## Supplementary materials

Supplementary material associated with this article can be found, in the online version, at doi:10.1016/j.cclet.2021.07.055.

## References

[1] B.C. Hodges, E.L. Cates, J.H. Kim, Nat. Nanotechnol. 13 (2018) 642–650.
[2] Y. Shang, X. Xu, B. Gao, S. Wang, X. Duan, Chem. Soc. Rev. 50 (2021) 5281–5322.
[3] M. Du, Q. Yi, J. Ji, et al., Chin. Chem. Lett. 31 (2020) 2803–2808.
[4] G. Yu, Y. Wang, H. Cao, H. Zhao, Y. Xie, Environ. Sci. Technol. 54 (2020) 5931–5946.
[5] Y. Wang, X. Duan, Y. Xie, H. Sun, S. Wang, ACS Catal. 10 (2020) 13383–13414.
[6] J. Wang, H. Chen, Sci. Total Environ. 704 (2020) 135249.
[7] Y. Wang, Y. Xie, H. Sun, et al., J. Hazard. Mater. 301 (2016) 56–64.
[8] F. Nawaz, H. Cao, Y. Xie, et al., Chemosphere 168 (2017) 1457–1466.
[9] C. Cai, X. Duan, X. Xie, et al., J. Hazard. Mater. 410 (2021) 124604.
[10] J. Ma, C. Wang, H. He, Appl. Catal. B: Environ. 201 (2017) 503–510.
[11] Y. Wang, Z. Chi, C. Chen, et al., Appl. Catal. B: Environ. 272 (2020) 118972.
[12] L. Zhang, Y. Shi, Y. Wang, N.R. Shiju, Adv. Sci. 7 (2020) 1902126.
[13] H. Qiu, P. Guo, L. Yuan, G. Sheng, Chin. Chem. Lett. 31 (2020) 2614–2618.
[14] Z. Liu, J. Ma, Y. Cui, B. Zhang, Appl. Catal. B: Environ. 92 (2009) 301–306.
[15] J. Peng, Y. He, C. Zhou, S. Su, B. Lai, Chin. Chem. Lett. 32 (2021) 1626–1636.
[16] J. Wang, S. Chen, X. Quan, H. Yu, Chemosphere 190 (2018) 135–143.
[17] Z. Song, M. Wang, Z. Wang, et al., Environ. Sci. Technol. 53 (2019) 5337–5348.
[18] Y. Shang, X. Xu, Q. Yue, B. Gao, Y. Li, Environ. Sci. Nano 7 (2020) 1444–1453.
[19] Z. Zhou, L. Miao, H. Duan, et al., Gan, Chin. Chem. Lett. 31 (2020) 1226–1230.
[20] Z. Song, Y. Zhang, C. Liu, et al., Chem. Eng. J. 357 (2019) 655–666.
[21] Z. Sun, L. Zhao, C. Liu, Y. Zhen, J. Ma, Environ. Sci. Technol. 53 (2019) 10342–10351.
[22] X. Duan, K. O'Donnell, H. Sun, Y. Wang, S. Wang, Small 11 (2015) 3036–3044.
[23] L. Zhou, Y. Xie, H. Cao, et al., Chem. Eng. J. 370 (2019) 208–217.
[24] W. Ren, G. Nie, P. Zhou, et al., Environ. Sci. Technol. 54 (2020) 6438–6447.
[25] H. Li, Y. Su, W. Sun, Y. Wang, Adv. Funct. Mater. 26 (2016) 8345–8353.
[26] Y. Qiu, J. Huo, F. Jia, B.H. Shanks, W. Li, J. Mater. Chem. A 4 (2016) 83–95.
[27] Y. Wang, N. Ren, J. Xi, et al., ACS ES&T Eng. 1 (2021) 32–45.
[28] J. Qian, X. Gao, B. Pan, Environ. Sci. Technol. 54 (2020) 8509–8526.
[29] L. Zhang, C. Lin, D. Zhang, et al., Adv. Mater. 31 (2019) 1805252.
[30] Y. Sun, J.J. Pignatello, Environ. Sci. Technol. 29 (1995) 2065–2072.
[31] T.M. El-Morsi, W.R. Budakowski, A.S. Abd-El-Aziz, K.J. Friesen, Environ. Sci. Technol. 34 (2000) 1018–1022.
[32] J. Ma, N.J.D. Graham, Water Res. 34 (2000) 3822–3828.
[33] J.L. Acero, U.v. Gunten, Ozone Sci. Eng. 22 (2000) 305–328.
[34] J.J. Wu, M. Muruganandham, S.H. Chen, J. Hazard. Mater. 149 (2007) 218–225.
[35] A.A. Frimer, Chem. Rev. 79 (1979) 359–387.
[36] W.H. Koppenol, D.M. Stanbury, P.L. Bounds, Free Radic. Biol. Med. 49 (2010) 317–322.
[37] F.E. Scully, J. Hoigné, Chemosphere 16 (1987) 681–694.
[38] F. Nawaz, Y. Xie, H. Cao, et al., Catal. Today 258 (2015) 595–601.
[39] Y. Nosaka, A.Y. Nosaka, Chem. Rev. 117 (2017) 11302–11336.
[40] P. Bilski, K. Reszka, M. Bilska, C.F. Chignell, J. Am. Chem. Soc. 118 (1996) 1330–1338.
[41] Y. Wang, L. Chen, C. Chen, et al., Appl. Catal. B: Environ. 254 (2019) 283–291.
[42] X. Chen, W.-D. Oh, Z. Hu, et al., Appl. Catal. B: Environ. 225 (2018) 243–257.
[43] G.V. Buxton, C.L. Greenstock, W.P. Helman, A.B. Ross, J. Phys. Chem. Ref. Data 17 (1988) 513–886.